

Sensorless Drive of Surface-Mounted Permanent-Magnet Motor by High-Frequency Signal Injection Based on Magnetic Saliency

Ji-Hoon Jang, *Student Member, IEEE*, Seung-Ki Sul, *Fellow, IEEE*, Jung-Ik Ha, *Member, IEEE*, Kozo Ide, *Member, IEEE*, and Mitsujiro Sawamura

Abstract—This paper presents a new sensorless control scheme of a surface-mounted permanent-magnet (SMPM) motor using high-frequency voltage signal injection method based on the high-frequency impedance difference. In the SMPM motor, due to the flux of the permanent magnet, the stator core around the q -axis winding is saturated. This makes the magnetic saliency in the motor. This magnetic saliency has the information about the rotor position. The high-frequency voltage signal is injected into the motor in order to detect the magnetic saliency and estimate the rotor position. In this paper, the relationship between the high-frequency voltages and high-frequency currents is developed using the voltage equations at the high frequency, and the high-frequency impedance characteristics are analyzed experimentally under various conditions. The proposed sensorless control scheme makes it possible to drive the SMPM motor in the low-speed region including zero speed, even under heavy load conditions. The experimental results verify the performance of the proposed sensorless algorithm.

Index Terms—High-frequency signal injection, sensorless drive, surface-mounted permanent-magnet (SMPM) motor.

I. INTRODUCTION

RECENTLY, with the advent of high-performance permanent magnets with high coercivity and high residual flux, it has been possible for the permanent-magnet (PM) motors to be superior to general-purpose induction motors in power density, torque-to-inertia ratio, and efficiency. Therefore, the PM motors are of more and more interest in many industrial applications as substitutes for induction motors. Besides the aforementioned advantages, the vector control of PM motors is much simpler than that of induction motors because there is no need to consider the slip frequency as in induction motor drive. However, PM motor drives require position sensors or rotational transducers to perform the vector control correctly because the rotor flux is obtained from permanent magnets. These position

sensors or rotational transducers not only increase cost, maintenance, and complexity, but also impair robustness and reliability of the drive system. Therefore, many researchers have been studying the sensorless drive of the PM motor in view of the robustness, reliability, cost, and so on [1].

Conventional sensorless control schemes of the PM motor can be classified into two types. The one is based on the back electromotive force (EMF) voltage estimation [2]–[10]. In this type, voltage model [2]–[4], state observer [5], [6], [10], or Kalman filters [7]–[9] have been used. In voltage model methods [2]–[4], the measured voltage and currents are used to estimate the position of rotor flux linkage based on the voltage equations of the PM motor. Parameter variations due to temperature and saturation critically affect the performance of the estimation of rotor position. In state observer and Kalman filter methods [5]–[10], the parameter variation effect is not as critical as in voltage model methods. However, the common problem of the above-mentioned methods is that the performance of the rotor position estimation is critically dependent on the magnitude of back-EMF voltage which is proportional to the rotor speed. In low-speed regions, where the magnitude of back-EMF voltage is so small, the performance is significantly degraded. In [10], a fluctuating high-frequency current signal injection is used to solve this problem. The basic idea of this method is to detect the small fluctuation of the back-EMF voltage by injecting a high-frequency test current to the machine at standstill. Using this method, maximum torque starting capability can be obtained in the sensorless drive of the PM motor. However, this method is valid only if the motor is connected to the load by the flexible coupling. The other is based on the magnetic saliency [11]–[14]. The basic idea of these schemes is injecting some extra voltage or current signals into the motor and using the corresponding signals to detect the rotor position. Some algorithms inject voltage signals in a sampling period to the motor [11]. Since the methods detect the inductance of the motor using voltage signals in a short time, they might be insignificant to the parameter variation and measurement noise. Also, due to the injected signal in this method being a periodic signal, a compensation scheme, such as a Kalman filter, is required. Another algorithm injects the rotating high-frequency voltage signals and uses a tracking algorithm [12]. Since it utilizes the rotating high-frequency signal, the dynamic characteristics are restricted in relation to the frequency of the injected signal. The fluctuating high-frequency voltage signal injection method [13], [14] shows good

Paper IPCSD 03–023, presented at the 2002 IEEE Applied Power Electronics Conference and Exposition, Dallas, TX, March 10–14, and approved for publication in the IEEE TRANSACTIONS ON INDUSTRY APPLICATIONS by the Industrial Drives Committee of the IEEE Industry Applications Society. Manuscript submitted for review June 1, 2002 and released for publication April 10, 2003.

J.-H. Jang and S.-K. Sul are with the School of Electrical Engineering and Computer Science, Seoul National University, Seoul 151-744, Korea (e-mail: bluemat@eepl.snu.ac.kr; sulsk@plaza.snu.ac.kr).

J.-I. Ha is with the Mechatronics Center, Samsung Electronics Company, Suwon 442-742, Korea (e-mail: haji@ieee.org).

K. Ide and M. Sawamura are with the Mechatronics R&D Department, Corporate R&D Center, Yaskawa Electric Company, Kitakyushu 803-8530, Japan (e-mail: kozo@yaskawa.co.jp).

Digital Object Identifier 10.1109/TIA.2003.813734

performance in the low-speed region including zero speed under loaded condition. However, it is used in the interior PM (IPM) motor. The common problem of the conventional sensorless control is that it cannot be applied to the sensorless drive of a surface-mounted PM (SMPM) motor at low and zero speed under heavy-load condition.

This paper presents a sensorless control scheme of an SMPM motor using high-frequency fluctuating voltage signal injection method based on the high-frequency impedance difference due to the magnetic saliency. Since it uses the high-frequency current signal corresponding to the high-frequency impedance difference of the SMPM motor to estimate the rotor position, the relationship between the rotor position estimation error and high-frequency current signal has been investigated. Also, the high-frequency impedance characteristics of the SMPM motor have been tested and analyzed under various conditions. In sensorless control, the high-frequency fluctuating voltage signal is injected on the d axis in the estimated synchronous reference frame, and the q -axis component of high-frequency current in the estimated synchronous reference frame is used to estimate the rotor position. The proposed rotor position estimation algorithm enables sensorless torque, speed, and position control under loaded condition. Experimental results verify the fast and accurate operation of the proposed sensorless algorithm.

II. ANALYSIS OF HIGH-FREQUENCY IMPEDANCE OF SMPM MOTOR

A. Relationship Between the High-Frequency Voltage and Current Signals

The voltage equations of the SMPM motor in the synchronous reference frame are represented as follows:

$$\begin{aligned} v_{ds}^r &= R_s i_{ds}^r + L_s \frac{d}{dt} i_{ds}^r - \omega_r L_s i_{qs}^r \\ v_{qs}^r &= R_s i_{qs}^r + L_s \frac{d}{dt} i_{qs}^r + \omega_r (L_s i_{ds}^r + K_e) \end{aligned} \quad (1)$$

where K_e is the back-EMF constant in volt-seconds per radian.

If the injected high-frequency component of voltages and currents are only considered and the injection frequency is sufficiently higher than the rotor speed of the SMPM motor in (1), the SMPM motor can be considered as a simple R - L load and the voltage equations can be represented as follows:

$$\begin{aligned} v_{dsh}^r &= r_{dh} i_{dsh}^r + L_{dh} \frac{d}{dt} i_{dsh}^r \\ v_{qsh}^r &= r_{qh} i_{qsh}^r + L_{qh} \frac{d}{dt} i_{qsh}^r. \end{aligned} \quad (2)$$

In (2), v_{dsh}^r and v_{qsh}^r are d - and q -axes high-frequency components of voltages in the actual synchronous reference frame, respectively. Also, i_{dsh}^r and i_{qsh}^r are d - and q -axes high-frequency components of currents in the actual synchronous reference frame, respectively. r_{dh} , r_{qh} and L_{dh} , L_{qh} are d - and q -axes resistances and inductances in the actual synchronous

reference frame at the injected high frequency, respectively. Furthermore, in the steady state, (2) can be expressed as (3)

$$\begin{aligned} v_{dsh}^r &= (r_{dh} + j\omega_h L_{dh}) i_{dsh}^r \equiv z_{dh}^r i_{dsh}^r \\ v_{qsh}^r &= (r_{qh} + j\omega_h L_{qh}) i_{qsh}^r \equiv z_{qh}^r i_{qsh}^r \end{aligned} \quad (3)$$

where z_{dh}^r and z_{qh}^r are d - and q -axes high-frequency impedances, respectively, and ω_h is injected high frequency in radians per second.

If the rotor position estimation error is defined as (4), the relationship between the high-frequency voltages and currents in the estimated synchronous reference frame can be expressed as follows based on the coordinate transform theory (see the Appendix):

$$\tilde{\theta}_r \equiv \theta_r - \hat{\theta}_r \quad (4)$$

where $\hat{\theta}_r$ is the estimated rotor position

$$\begin{bmatrix} \hat{i}_{dsh}^r \\ \hat{i}_{qsh}^r \end{bmatrix} = \begin{bmatrix} \cos \tilde{\theta}_r & -\sin \tilde{\theta}_r \\ \sin \tilde{\theta}_r & \cos \tilde{\theta}_r \end{bmatrix} \begin{bmatrix} 1/z_{dh}^r & 0 \\ 0 & 1/z_{qh}^r \end{bmatrix} \cdot \begin{bmatrix} \cos \tilde{\theta}_r & \sin \tilde{\theta}_r \\ -\sin \tilde{\theta}_r & \cos \tilde{\theta}_r \end{bmatrix} \begin{bmatrix} \hat{v}_{dsh}^r \\ \hat{v}_{qsh}^r \end{bmatrix} \quad (5)$$

where \hat{v}_{dsh}^r and \hat{v}_{qsh}^r are d - and q -axes high-frequency components of voltages in the estimated synchronous reference frame, and \hat{i}_{dsh}^r and \hat{i}_{qsh}^r are d - and q -axes high-frequency components of currents, respectively, in the estimated synchronous reference frame.

If the average and difference of d - and q -axes high-frequency impedances is defined as (6), (5) can be rewritten as (7)

$$z_{\text{avg}} \equiv \frac{z_{dh}^r + z_{qh}^r}{2}, \quad z_{\text{diff}} \equiv z_{dh}^r - z_{qh}^r \quad (6)$$

where z_{avg} is the average of d - and q -axes high-frequency impedances, and z_{diff} is the difference between d - and q -axes high-frequency impedances

$$\begin{aligned} \hat{i}_{dsh}^r &= \frac{1}{z_{dh}^r z_{qh}^r} \left[\left(z_{\text{avg}} - \frac{1}{2} z_{\text{diff}} \cos 2\tilde{\theta}_r \right) \hat{v}_{dsh}^r \right. \\ &\quad \left. - \left(\frac{1}{2} z_{\text{diff}} \sin 2\tilde{\theta}_r \right) \hat{v}_{qsh}^r \right] \\ \hat{i}_{qsh}^r &= \frac{1}{z_{dh}^r z_{qh}^r} \left[\left(-\frac{1}{2} z_{\text{diff}} \sin 2\tilde{\theta}_r \right) \hat{v}_{dsh}^r \right. \\ &\quad \left. + \left(z_{\text{avg}} + \frac{1}{2} z_{\text{diff}} \cos 2\tilde{\theta}_r \right) \hat{v}_{qsh}^r \right]. \end{aligned} \quad (7)$$

Therefore, if the fluctuating high-frequency voltage signal is injected only on the d axis in the estimated synchronous reference frame as in (8), the resultant high-frequency currents can be represented as (9)

$$\begin{aligned} \hat{v}_{dsh}^r &= V_{inj} \cos \omega_h t, \quad \hat{v}_{qsh}^r = 0 \\ \hat{i}_{dsh}^r &= \frac{V_{inj} \cos \omega_h t}{z_{dh}^r z_{qh}^r} \left(z_{\text{avg}} - \frac{1}{2} z_{\text{diff}} \cos 2\tilde{\theta}_r \right) \\ \hat{i}_{qsh}^r &= \frac{V_{inj} \cos \omega_h t}{z_{dh}^r z_{qh}^r} \left(-\frac{1}{2} z_{\text{diff}} \sin 2\tilde{\theta}_r \right). \end{aligned} \quad (8) \quad (9)$$

TABLE I
PARAMETERS OF TESTED SMPM MOTOR

Rated Power	11 [kW]
Rated Torque	70 [Nt-m]
Number of Poles	8
Rated Voltage	180 [V(rms)]
Rated Current	58.6 [A(rms)]
Rated Speed	1500 [r/min]
Torque Coefficient	1.25 [Nt-m/A(rms)]
Inertia	0.0281 [kg-m ²]
Resistance(per phase)	0.0217 [Ω]
Inductance(per phase)	0.49 [mH]

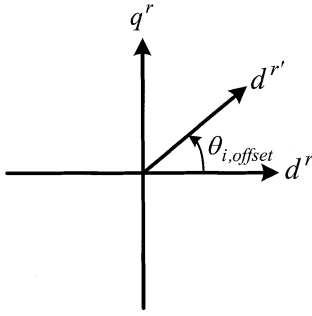


Fig. 1. Relationship between the measurement axis and the actual axis.

From (9), it can be known that the d - and q -axes high-frequency components of currents in the estimated synchronous reference frame have the information about the rotor position estimation error if the high-frequency impedance difference between d and q axes is not zero ($z_{diff} \neq 0$). The d -axis high-frequency current is offset by average high-frequency impedance, and is not zero even if the rotor position estimation error is zero. On the contrary, the q -axis high-frequency current becomes zero when the rotor position estimation error is zero. Therefore, in this paper, the q -axis high-frequency current in (9) is used as an input signal to the rotor position estimator in order to estimate rotor position and speed.

B. Measurement of High-Frequency Impedance of SMPM Motor

In the above section, the information about the rotor position estimation error can be obtained through a high-frequency current in the estimated synchronous reference frame if the high-frequency impedance difference is not zero. Therefore, in this paper, to investigate the high-frequency impedance characteristics of an SMPM motor, some impedance measurement tests have been performed. The motor under test is a commercial 11-kW SMPM motor, and has the parameters as shown in Table I. Fig. 1 shows the relationship between the actual axes and the measurement axis. In the measurement of the high-frequency impedance test, the rotor of SMPM motor is mechanically locked to prevent the distortion of the signal by the back-EMF voltage due to the rotor vibration. In Fig. 1, the $d^{r'}$ axis is the measurement axis, and $\theta_{i,offset}$ is the relative position of measurement axis to the actual d axis, which is

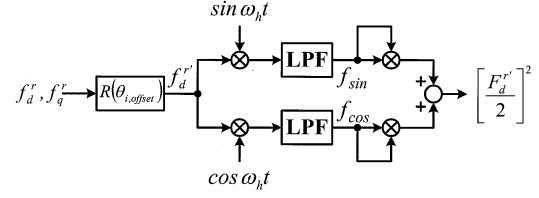


Fig. 2. Procedure of signal processing to measure the magnitude of high-frequency variables.

negative in the sense of the rotor position estimation error in (4) by its definition.

Fig. 2 shows the procedure of the signal processing to calculate the magnitude of high-frequency variables. In Fig. 2, $R(\theta)$ is a coordinate transform operator which can be expressed as in (10), and “ f ” can be voltages or currents. If “ f ” can be represented in (11), its magnitude can be obtained through the signal processing from (12)–(14). In (12) and (13), $\text{LPF}(\cdot)$ means a low-pass filter

$$R(\theta) = \begin{bmatrix} \cos \theta & \sin \theta \\ -\sin \theta & \cos \theta \end{bmatrix} \quad (10)$$

$$f = F_d^{r'} \sin(\omega_h t + \phi) = (F_d^{r'} \cos \phi) \sin \omega_h t + (F_d^{r'} \sin \phi) \cos \omega_h t \quad (11)$$

$$f_{\sin} \equiv \text{LPF}(f \sin \omega_h t) = \frac{F_d^{r'} \cos \phi}{2} \quad (12)$$

$$f_{\cos} \equiv \text{LPF}(f \cos \omega_h t) = \frac{F_d^{r'} \sin \phi}{2} \quad (13)$$

$$F_d^{r'} = 2\sqrt{(f_{\sin})^2 + (f_{\cos})^2}. \quad (14)$$

Therefore, the magnitude of high-frequency voltage and current, and the high-frequency impedance on the measurement axis, can be obtained as follows:

$$V_d^{r'} = 2\sqrt{(v_{\sin})^2 + (v_{\cos})^2} \quad (15)$$

$$I_d^{r'} = 2\sqrt{(i_{\sin})^2 + (i_{\cos})^2} \quad (16)$$

$$Z_d^{r'} = \frac{V_d^{r'}}{I_d^{r'}}. \quad (17)$$

Figs. 3–5 show the measurement results of high-frequency impedance of the tested SMPM motor at various operating conditions. In the figures, “Test_angle” is the relative position of measurement axis to the actual d axis, and it means the “ $\theta_{i,offset}$ ” in Fig. 1. Therefore, when “Test_angle” is zero, the high-frequency voltage signal is injected into the d axis. Fig. 3 shows the high-frequency impedance characteristics at various magnitudes of the injected high-frequency voltage signal where the injection frequency is 550 Hz. As can be seen in the figure, the d -axis high-frequency impedance is larger than that of the q axis. The high-frequency impedance differences (z_{diff}) between d and q axes are about 30% of the average impedance (z_{avg}) at all magnitudes of the injected high-frequency voltage signals. As the magnitude is increased, the d -axis high-frequency impedance decreases, but the q -axis high-frequency impedance does not decrease. This is due to the fact that the stator core around the q -axis winding is already saturated. Therefore, increasing the magnitude of the injected voltage signal cannot affect the q -axis high-frequency impedance.

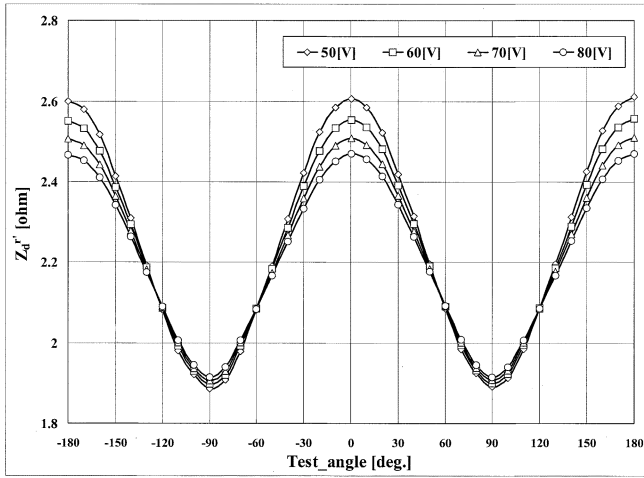


Fig. 3. High-frequency impedance characteristics at various injection voltages (550 Hz).

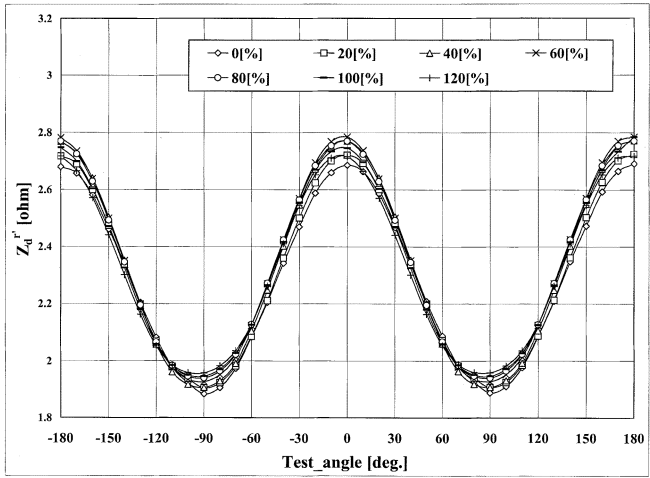


Fig. 5. High-frequency impedance characteristics under various load torques (40 V, 550 Hz).

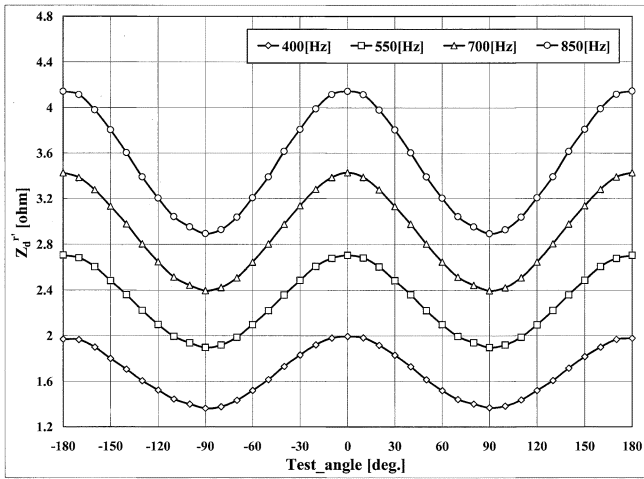


Fig. 4. High-frequency impedance characteristics at various injection frequencies ($V/f = 40 \text{ V}/550 \text{ Hz}$).

Fig. 4 shows the high-frequency impedance characteristics at various frequencies of the injected voltage signal. In this test, the ratio of the magnitude to frequency of the injected high-frequency voltage signal has been maintained to constant in order to make the magnitude of high-frequency current be constant. From Fig. 4, it can be known that the high-frequency impedance is mainly due to the inductance, because the magnitude of the high-frequency impedance increases as the frequency of the injected high-frequency voltage signal is increased. As in Fig. 3, the differences between d - and q -axes high-frequency impedance is about 30% of the average impedance at all injection frequencies. Fig. 5 shows the high-frequency impedance characteristics under various load torques. The magnitude and frequency of the injected high-frequency voltage signal are 40 V and 550 Hz, respectively. Even under the heavy loaded conditions, the high-frequency impedance difference does not disappear. It is about 30% of the average high-frequency impedance. However, as the load torque increases, the difference between d - and q -axes high-frequency impedance slightly decreases.

III. CONTROL SCHEME USING THE HIGH-FREQUENCY CURRENT

A. Calculation of Input Signal to Rotor Position Estimator

The high-frequency currents in the estimated synchronous reference frame in (9) have the information about the rotor position estimation error. In this paper, the high-frequency current on the q axis in the estimated synchronous reference frame has been used because it does not have the average high-frequency impedance components, which is an offset, and it is proportional to the sine of two times rotor position estimation error, which is an odd function. By assuming that the high-frequency impedance due to the high-frequency resistance is sufficiently smaller than the high-frequency impedance itself due to the high-frequency inductance as in (18), the q -axis high-frequency current in (9) can be rewritten as in (19) in the steady state

$$\begin{aligned} z_{dh}^r &= r_{dh} + j\omega_h L_{dh} \approx j\omega_h L_{dh} \\ z_{qh}^r &= r_{qh} + j\omega_h L_{qh} \approx j\omega_h L_{qh} \end{aligned} \quad (18)$$

$$\hat{i}_{qsh}^r = \frac{V_{inj} \sin 2\tilde{\theta}_r}{2\omega_h^2 L_{dh} L_{qh}} [r_{diff} \cos \omega_h t - L_{diff} \sin \omega_h t] \quad (19)$$

where r_{diff} is the difference between the d - and q -axes high-frequency resistances, and L_{diff} is the difference between the d - and q -axes high-frequency inductances.

From (19), the input signal to the rotor position estimator can be obtained via signal process as in (20)

$$\hat{i}_{\tilde{\theta}_r} \equiv \text{LPF} \left(\hat{i}_{qsh}^r \sin \omega_h t \right) = -\frac{V_{inj} L_{diff}}{4\omega_h L_{dh} L_{qh}} \sin 2\tilde{\theta}_r. \quad (20)$$

If the rotor position estimation error is sufficiently small, the input signal in (20) can be linearized as (21)

$$\hat{i}_{\tilde{\theta}_r} \approx -\frac{V_{inj} L_{diff}}{2\omega_h L_{dh} L_{qh}} \tilde{\theta}_r \equiv K_{err} \tilde{\theta}_r. \quad (21)$$

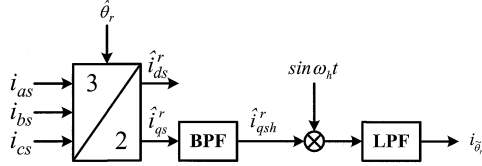


Fig. 6. Procedure of signal processing to calculate the input signal to the rotor position estimator.

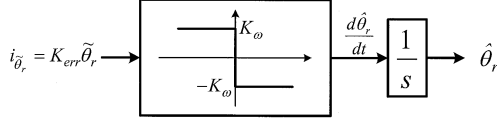


Fig. 7. Block diagram of the proposed rotor position estimator.

Fig. 6 shows the procedure of signal processing to calculate the input signal of the rotor position estimator. It consists of a band-pass filter (BPF), a multiplication, and a low-pass filter (LPF). The coordinate transform which transforms the current from the three-phase reference frame to the estimated synchronous reference frame is the same as that is used in the current control. It is much simpler than the method using two measurement axes which are 45° apart from the estimated synchronous reference frame in [13] or the method using the fast Fourier transform (FFT) algorithm and phase-locked loop (PLL) algorithm in [14].

B. Proposed Rotor Position Estimator

Fig. 7 shows the block diagram of the proposed rotor position estimator. It consists of a bang-bang controller with an integrator. The output of the bang-bang controller is positive if the input is negative and vice versa. The magnitude of the output of the bang-bang controller is determined by the K_ω , so the maximum rotor position estimation error and the dynamic characteristics of the rotor position estimator of this type are determined by the K_ω . The bang-bang controller type of estimator has the disadvantages that the actuation of the bang-bang controller makes some ripples in speed and torque, and that the rotor position estimation error is not zero instantaneously. However, it has advantages such as fast dynamic characteristics and very simple structure. Also, the torque ripple, due to the fluctuation of the estimated rotor position of the bang-bang controller, does not impair the performance of torque, speed, and position control.

C. Proposed Rotor Speed Estimator

In a PM motor, there is no slip frequency as in an induction motor, regardless of the output torque. Therefore, the rotor speed is equal to the time derivative of the rotor position. This makes the estimation of the rotor speed of the PM motor simpler than that of the induction motor.

Fig. 8 shows the block diagram of the proposed rotor speed estimator. It uses the output of the bang-bang controller in the rotor position estimator. The output of the bang-bang controller in the rotor position estimator has the same dimension as the rotor speed (see Fig. 7), so it can be directly used to estimate the rotor speed. However, due to the actuation of the bang-bang

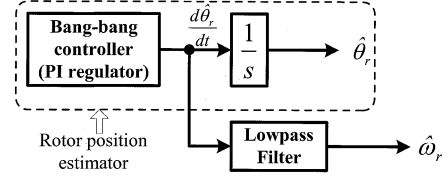


Fig. 8. Block diagram of the proposed rotor speed estimator.

controller, its output has large ripples, which may impair the performance of the speed control. Therefore, an LPF is used to reduce the ripple in the estimated rotor speed. In this paper, the cutoff frequency of the LPF is set to 100 rad/s.

IV. EXPERIMENTAL RESULTS

A. System Configuration

The experiments to verify the proposed sensorless control algorithm have been performed using a commercial SMPM motor, which is the same motor that has been used in the high-frequency impedance measurement tests. In Fig. 9, the experimental system configuration is presented. Fig. 9(a) shows the block diagram of the sensorless drive system of the SMPM motor including the proposed sensorless control algorithm. It consists of the high-frequency voltage signal injection, position, speed, and current controller, pulsewidth modulation (PWM) voltage-source inverter (VSI), digital LPFs to extract the fundamental components of currents, and the proposed sensorless control algorithm shown in Figs. 6–8. In the figure, \hat{i}_{dqs1}^r is the d - and q -axes fundamental components of currents in the estimated synchronous reference frame, which are used in the current controller. The position controller is a proportional controller, which does not have overshoot in the output. The speed controller and current controller are conventional proportional–integral (PI) controllers with antiwindup. Also, the d -axis current command in the synchronous reference frame is usually set to zero. The PWM VSI consists of an intelligent power module, and is controlled by the control board using a digital signal processor (DSP), TMS320VC33 100 MHz. The PWM switching frequency is 5 kHz, and the sampling frequency is 10 kHz. As in Fig. 9(a), the high-frequency voltage signal is injected through the space-vector PWM. The high-frequency voltage signal is added to the output of the current controller in the DSP. In the experiments, the magnitude and frequency of the high-frequency voltage signal are 100 V and 850 Hz.

Fig. 9(b) shows the experimental setup. The tested SMPM motor (SMPMM) is a commercial motor made by Yaskawa Electric Company. This motor does not have any saliency in the fundamental frequency region. An 11-kW induction motor (IM) has been used in order to apply the load torque.

B. Performance of Torque Control

Fig. 10 shows the performance of torque control of the proposed sensorless control algorithm. In this experiment, the speed command of the load machine is maintained constant as -50 r/min, and the torque command of the tested SMPM motor

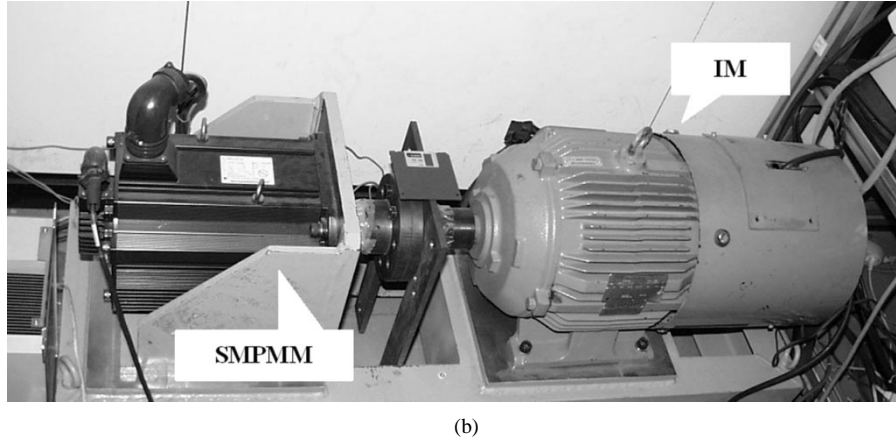
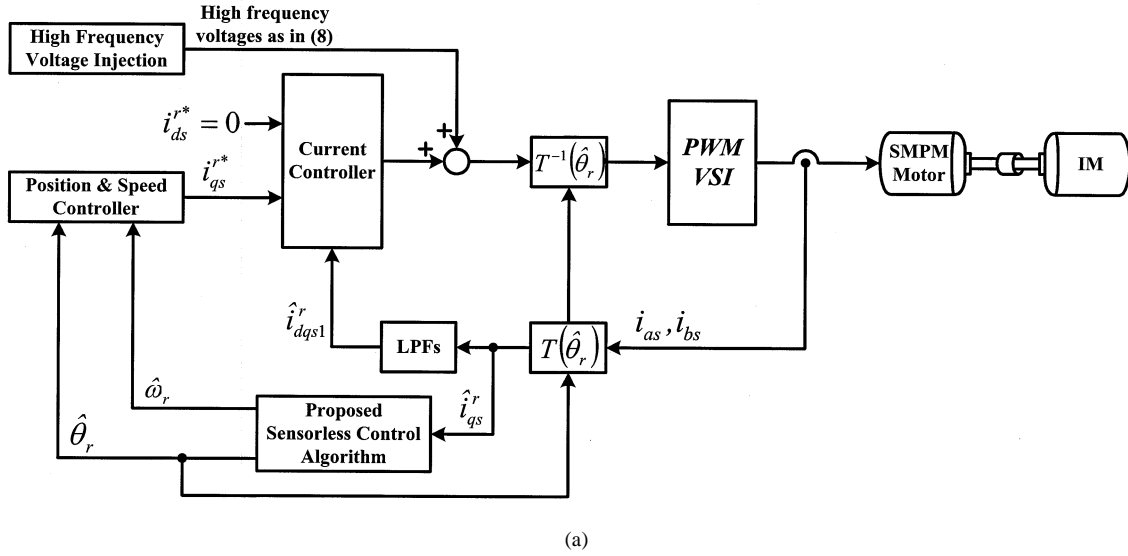


Fig. 9. System configuration for the experiments. (a) Block diagram of the proposed sensorless drive system. (b) Experimental setup.

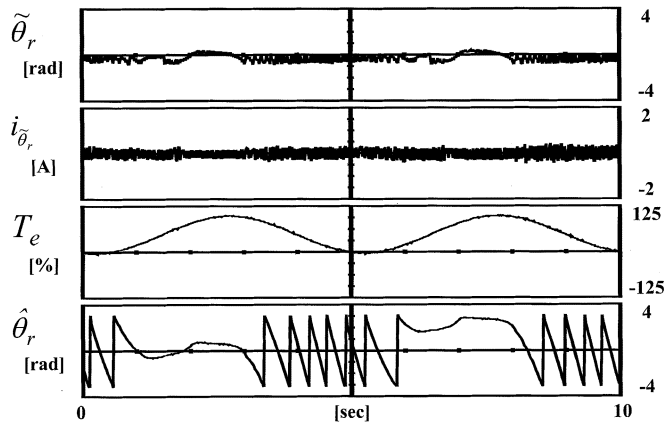


Fig. 10. Performance of the proposed algorithm with a positive torque command at negative constant speed. (From top to bottom: estimation error, the signal for angle error, measured torque, and estimated rotor position.)

has been changed in sinusoidal shape. The torque command in the experiments of Fig. 10 can be expressed as in (22)

$$T_e^* = 0.5 \times T_{e, \text{rate}} [\sin(\omega t) + 1] \quad (22)$$

where $T_{e, \text{rate}}$ is the rated torque of the tested SMPM motor.

In the figure, rotor position estimation error ($\tilde{\theta}_r$) in radians, input signal to the rotor position estimator ($i_{\tilde{\theta}_r}$) in amperes, output torque of the SMPM motor (T_e) in percentage ratio to the rated torque, and the estimated rotor position ($\hat{\theta}_r$) in radians are presented. Although the speed command of the load machine is constant, the speed is fluctuating when the torque command of the SMPM motor is increased due to the slow dynamic characteristics of the speed controller of the load machine. The maximum instantaneous rotor position estimation error is about 0.7~0.8 rad, but the average rotor position estimation error is confined within a narrow limit even under heavy-load torque condition.

C. Performance of Speed Control

The experimental results of the proposed sensorless speed control algorithm are shown in Figs. 11 and 12. In the figures, measured rotor speed (ω_{rpm}) in revolutions per minute, estimated rotor position ($\hat{\theta}_r$) in radians, rotor position estimation error ($\tilde{\theta}_r$) in radians, and the output torque of the SMPM motor (T_e) in percentage ratio to the rated torque are presented. Fig. 11 shows the performance of the proposed sensorless speed control algorithm with zero-speed command under 100% step load torque condition. Even though there are some ripples in torque

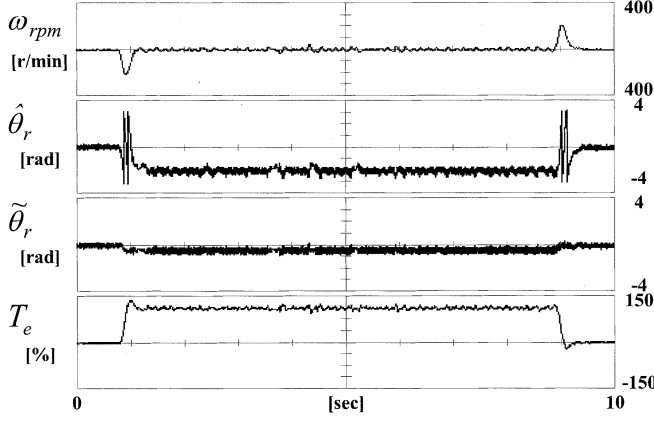


Fig. 11. Performance of the proposed algorithm with command under 100% step load torque. (From top to bottom: measured speed, estimated rotor position, rotor position estimation error, and measured torque.)

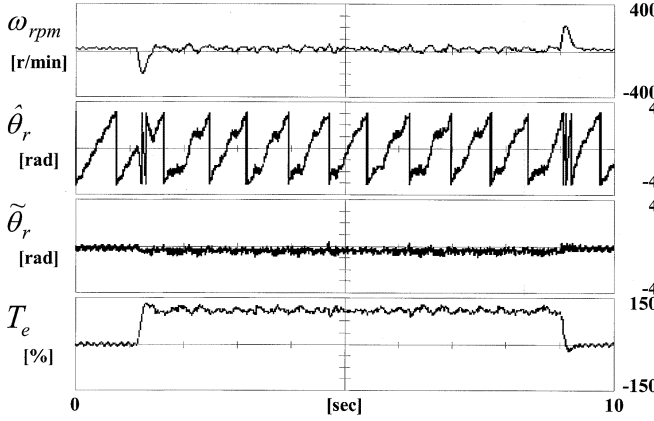


Fig. 12. Performance of the proposed algorithm with 20-r/min command under 100% step load torque. (From top to bottom: measured speed, estimated rotor position, rotor position estimation error, and measured torque.)

and speed in the steady state when the load torque is applied, the proposed sensorless speed control algorithm does not lose the estimation and control capability, and the rotor position estimation error is confined to nearly zero in the transient state as well as in the steady state. Fig. 12 shows the performance of the proposed algorithm with 20-r/min speed command under 100% step load torque condition. The SMPM motor has eight poles, so 20 r/min means that the rotor frequency is about 1.3 Hz, which is very low frequency because the rated rotor frequency of the SMPM motor is 100 Hz. Compared to the zero-speed operation, the torque ripple is somewhat increased. This ripple is not from the proposed sensorless speed control algorithm, but it is mainly caused by the disturbances such as dead-time effect and zero crossing of the phase currents. Figs. 11 and 12 show that the proposed sensorless speed control algorithm enables the speed control in the low-speed region including zero speed without any position or speed sensor.

D. Performance of Position Control

The experimental results of the proposed sensorless position control algorithm are shown in Figs. 13 and 14. In the figures, measured rotor speed (ω_{rpm}) in revolutions per minute, estimated mechanical rotor position ($\hat{\theta}_{rm}$) in radians, the mechan-

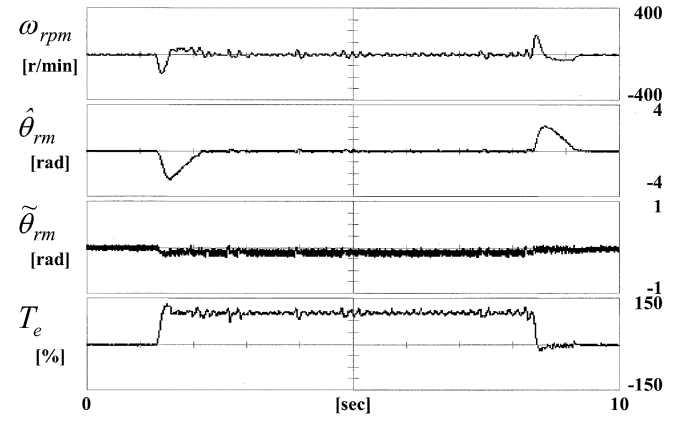


Fig. 13. Performance of the proposed algorithm with zero position command under 100% step load torque. (From top to bottom: measured speed, estimated rotor position, rotor position estimation error, and measured torque.)

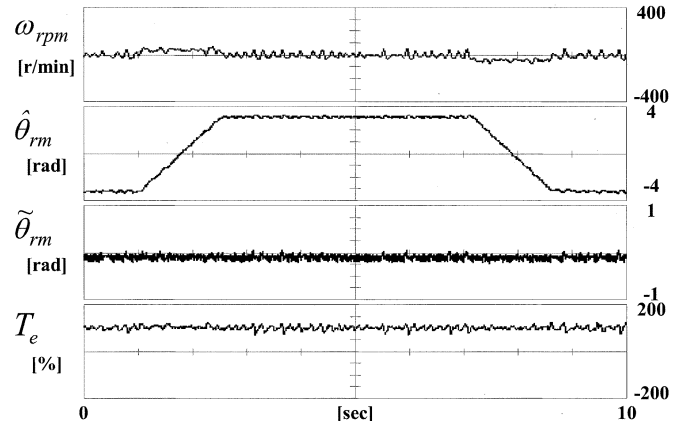


Fig. 14. Performance of the proposed algorithm with position command change from $-\pi \sim \pi$ radians in mechanical under 100% constant load torque. (From top to bottom: measured speed, estimated rotor position, rotor position estimation error, and measured torque.)

ical rotor position estimation error ($\tilde{\theta}_{rm}$) in radians, and the output torque of the SMPM motor (T_e) in percentage ratio to the rated torque are presented. Fig. 13 shows the performance of the proposed algorithm with zero position command under 100% step load torque condition. The rotor position estimation error is nearly zero in the steady state, and is confined within a narrow limit even in the transient state. Fig. 14 shows the performance of the proposed sensorless algorithm with the position command change from $-\pi$ to π rad mechanically (one revolution) under 100% constant load torque condition. Initially, the position command is set to $-\pi$ rad, and changed to π rad mechanically during 1.5 s, and then returned to $-\pi$ rad. In measured speed and output torque, there are some ripples. However, in the estimated rotor position, the ripple is very small.

V. CONCLUSIONS

In this paper, a new sensorless control algorithm of the SMPM motor using the high-frequency signal injection based on the high-frequency impedance difference has been proposed. In order to use the high-frequency impedance difference, the high-frequency impedance characteristics of an SMPM motor have been tested under various operating conditions. Based

on the characteristics, it is shown that the rotor position can be estimated using high-frequency component of currents on the q axis in the estimated synchronous reference frame if the direct (d) and quadrature (q) axes high-frequency impedances, mainly high-frequency inductances, are different. The proposed sensorless control algorithm contains a high-frequency voltage signal injection scheme, extraction of rotor position estimation error information from the high-frequency component of currents, rotor position estimator, and rotor speed estimator.

In order to verify the proposed sensorless algorithm, an experimental system using a commercial SMPM motor has been set up and tested. The experimental results clarify that the proposed sensorless control algorithm using the high-frequency voltage signal injection based on the high-frequency impedance difference enables torque, speed, and position control in the low-speed region including zero speed without any speed or position sensor under heavy-load condition.

APPENDIX

The high-frequency components of the voltage equations in (3) can be written as in (A.1). Therefore, the high-frequency components of currents can be expressed as in (A.2) through the inversion of a matrix

$$\begin{bmatrix} v_{dsh}^r \\ v_{qsh}^r \end{bmatrix} = \begin{bmatrix} z_{dh}^r & 0 \\ 0 & z_{qh}^r \end{bmatrix} \begin{bmatrix} i_{dsh}^r \\ i_{qsh}^r \end{bmatrix} \quad (\text{A.1})$$

$$\begin{bmatrix} i_{dsh}^r \\ i_{qsh}^r \end{bmatrix} = \begin{bmatrix} z_{dh}^r & 0 \\ 0 & z_{qh}^r \end{bmatrix}^{-1} \begin{bmatrix} v_{dsh}^r \\ v_{qsh}^r \end{bmatrix} \\ = \begin{bmatrix} 1/z_{dh}^r & 0 \\ 0 & 1/z_{qh}^r \end{bmatrix} \begin{bmatrix} v_{dsh}^r \\ v_{qsh}^r \end{bmatrix}. \quad (\text{A.2})$$

The relationship between the variables in the actual synchronous reference frame and variables in the estimated synchronous reference frame can be written as in (A.3) and (A.4)

$$\begin{bmatrix} f_d^r \\ f_q^r \end{bmatrix} = \begin{bmatrix} \cos \tilde{\theta}_r & \sin \tilde{\theta}_r \\ -\sin \tilde{\theta}_r & \cos \tilde{\theta}_r \end{bmatrix} \begin{bmatrix} \hat{f}_d^r \\ \hat{f}_q^r \end{bmatrix} \quad (\text{A.3})$$

$$\begin{bmatrix} \hat{f}_d^r \\ \hat{f}_q^r \end{bmatrix} = \begin{bmatrix} \cos \tilde{\theta}_r & -\sin \tilde{\theta}_r \\ \sin \tilde{\theta}_r & \cos \tilde{\theta}_r \end{bmatrix} \begin{bmatrix} f_d^r \\ f_q^r \end{bmatrix}. \quad (\text{A.4})$$

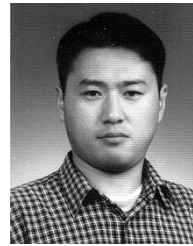
Equation (A.2) can be expressed as in (A.5) using (A.3) and (A.4)

$$\begin{bmatrix} \hat{i}_{dsh}^r \\ \hat{i}_{qsh}^r \end{bmatrix} = \begin{bmatrix} \cos \tilde{\theta}_r & -\sin \tilde{\theta}_r \\ \sin \tilde{\theta}_r & \cos \tilde{\theta}_r \end{bmatrix} \begin{bmatrix} i_{dsh}^r \\ i_{qsh}^r \end{bmatrix} \\ = \begin{bmatrix} \cos \tilde{\theta}_r & -\sin \tilde{\theta}_r \\ \sin \tilde{\theta}_r & \cos \tilde{\theta}_r \end{bmatrix} \begin{bmatrix} 1/z_{dh}^r & 0 \\ 0 & 1/z_{qh}^r \end{bmatrix} \begin{bmatrix} v_{dsh}^r \\ v_{qsh}^r \end{bmatrix} \\ = \begin{bmatrix} \cos \tilde{\theta}_r & -\sin \tilde{\theta}_r \\ \sin \tilde{\theta}_r & \cos \tilde{\theta}_r \end{bmatrix} \begin{bmatrix} 1/z_{dh}^r & 0 \\ 0 & 1/z_{qh}^r \end{bmatrix} \\ \cdot \begin{bmatrix} \cos \tilde{\theta}_r & \sin \tilde{\theta}_r \\ -\sin \tilde{\theta}_r & \cos \tilde{\theta}_r \end{bmatrix} \begin{bmatrix} \hat{v}_{dsh}^r \\ \hat{v}_{qsh}^r \end{bmatrix}. \quad (\text{A.5})$$

Equation (A.5) shows the relationship between the high-frequency components of currents and voltages in the estimated synchronous reference frame.

REFERENCES

- [1] P. Pillay and P. Freere, "Literature survey of permanent magnet AC motors and drives," in *Conf. Rec. IEEE-IAS Annu. Meeting*, 1991, pp. 74–84.
- [2] R. Wu and G. R. Slemon, "A permanent magnet motor drive without a shaft sensor," *IEEE Trans. Ind. Applicat.*, vol. 27, pp. 1005–1011, Sept./Oct. 1991.
- [3] M. Naidu and B. K. Bose, "Rotor position estimation scheme of a permanent magnet synchronous machine for high performance variable speed drive," in *Conf. Rec. IEEE-IAS Annu. Meeting*, 1992, pp. 48–53.
- [4] N. Ertugrul and P. Acarnley, "A new algorithm for sensorless operation of permanent magnet motors," *IEEE Trans. Ind. Applicat.*, vol. 30, pp. 126–133, Jan./Feb. 1994.
- [5] L. A. Jones and J. H. Lang, "A state observer for the permanent-magnet synchronous motor," *IEEE Trans. Ind. Electron.*, vol. 36, pp. 374–382, June 1989.
- [6] R. B. Sepe and J. H. Lang, "Real-time observer-based (adaptive) control of a permanent-magnet synchronous motor without mechanical sensors," *IEEE Trans. Ind. Applicat.*, vol. 28, pp. 1345–1352, Nov./Dec. 1992.
- [7] R. Dhauoadi, N. Mohan, and L. Norum, "Design and implementation of an extended Kalman filter for the state estimation of a permanent magnet synchronous motor," *IEEE Trans. Power Electron.*, vol. 6, pp. 491–497, May 1991.
- [8] J. Hu, D. Zhu, and B. Wu, "Permanent magnet synchronous motor drive without mechanical sensors," in *Conf. Rec. IEEE CCECE*, 1996, pp. 603–606.
- [9] S. Bolognani, R. Oboe, and M. Zigliotto, "Sensorless full-digital PMSM drive with EKF estimation of speed and rotor position," *IEEE Trans. Ind. Electron.*, vol. 46, pp. 184–191, Feb. 1999.
- [10] J. S. Kim and S. K. Sul, "New approach for high performance PMSM drives without rotational position sensors," *IEEE Trans. Power Electron.*, vol. 12, pp. 904–911, Sept. 1997.
- [11] M. Schroedl, "Sensorless control of AC machines at low speed and standstill based on the 'INFORM' method," in *Conf. Rec. IEEE-IAS Annu. Meeting*, 1996, pp. 270–277.
- [12] P. L. Jansen and R. D. Lorenz, "Transducerless position and velocity estimation in induction and salient AC machines," *IEEE Trans. Ind. Applicat.*, vol. 31, pp. 240–247, Mar./Apr. 1995.
- [13] J. I. Ha, S. K. Sul, and M. H. Park, "Position controlled interior permanent magnet motor without any rotational transducer," in *Conf. Rec. IEEE-2K*, 2000, pp. 396–399.
- [14] T. Aihara, A. Toba, T. Yanase, A. Mashimo, and K. Endo, "Sensorless torque control of salient-pole synchronous motor at zero-speed operation," *IEEE Trans. Power Electron.*, vol. 14, pp. 202–208, Jan. 1999.



Ji-Hoon Jang (S'01) was born in Seoul, Korea, in 1975. He received the B.S. and M.S. degrees in electrical engineering in 1999 and 2001, respectively, from Seoul National University, Seoul, Korea, where he is currently working toward the Ph.D. degree.

His research interests are high-performance ac machine drives, sensorless drives of ac machines, and electrical systems in vehicles.



Seung-Ki Sul (S'78–M'80–SM'98–F'00) was born in Korea in 1958. He received the B.S., M.S., and Ph.D. degrees in electrical engineering from Seoul National University, Seoul, Korea, in 1980, 1983, and 1986, respectively.

From 1986 to 1988, he was an Associate Researcher with the Department of Electrical and Computer Engineering, University of Wisconsin, Madison. From 1988 to 1990, he was a Principal Research Engineer with Gold-Star Industrial Systems Company. Since 1991, he has been a member of the faculty of the School of Electrical Engineering, Seoul National University, where he is currently a Professor. His current research interests are power-electronic control of electric machines, electric vehicle drives, custom powers, and power-converter circuits.



Jung-Ik Ha (S'97–M'01) was born in Pusan, Korea, in 1971. He received the B.S., M.S., and Ph.D. degrees in electrical engineering from Seoul National University, Seoul, Korea, in 1995, 1997, and 2001, respectively.

He was with the Mechatronics R&D Department of Yaskawa Electric Company, Japan, as a Researcher from 2001 to 2002. He is currently a Senior Research Engineer with the Mechatronics Center, Samsung Electronics Company, Suwon, Korea. His current research interests are electric machines,

drives, and electric propulsion systems.



Mitsujiro Sawamura was born in Japan. He received the B.S. degree in physics from Kumamoto University, Kumamoto City, Japan, in 1981.

In 1981, he joined Yaskawa Electric Company, Kitakyushu, Japan, where he is currently a Manager of the Control Technology Section. He is interested in sensorless control, spindle drives, and other drive application issues.

Mr. Sawamura is a member of the Institute of Electrical Engineers of Japan.



Kozo Ide (S'92–M'96) received the B.S., M.S., and Ph.D. degrees in electrical engineering from Kyushu Institute of Technology, Kitakyushu, Japan, in 1991, 1993, and 1996, respectively.

From 1991 to 1992, he was a Visiting Researcher at L'Aquila University, Italy, supported by the Italian government. In 1996, he joined Yaskawa Electric Company, Kitakyushu, Japan, where he is currently a Staff Engineer in the R&D Center. From 2002 to July 2003, he was a Visiting Researcher with Siemens AG, Germany. His current research interests are

control technology for ac machines and energy conversion systems.

Dr. Ide is a Member of the Institute of Electrical Engineers of Japan.